

Optical properties of deep ice at the South Pole: scattering

P. Buford Price and Lars Bergström

Recently, absorption and scattering at depths 800–1000 m in South Pole ice have been studied with transit-time distributions of pulses from a variable-frequency laser sent between emitters and receivers embedded in the ice. At 800–1000 m, scattering is independent of wavelength and the scattering centers are air bubbles of size \gg wavelength. At 1500–2000 m it is predicted that all bubbles will have transformed into air-hydrate clathrate crystals and that scattering occurs primarily at dust grains, at liquid acids concentrated along three-crystal boundaries, and at salt grains. Scattering on decorated dislocations, at ice–ice boundaries, and at hydrate–ice boundaries will be of minor importance. Scattering from liquid acids in veins at three-crystal boundaries goes as $\sim\lambda^{-1}$ to $\sim\lambda^{-2}$ and should show essentially no depth dependence. Scattering from dust grains goes as $\sim\lambda^{-2}$ and should show peaks at depths of ~ 1050 , ~ 1750 , and ~ 2200 m in South Pole ice. If marine salt grains remain undissolved, they will scatter like insoluble dust grains. Refraction at ice–ice boundaries and at hydrate–ice boundaries is manifested by a multitude of small-angle scatters, independent of wavelength. The largest contribution to Rayleigh-like scattering is likely due to dislocations decorated discontinuously with impurities. Freshly grown laboratory ice exhibits a large Rayleigh-like scattering that we attribute to the much higher density of decorated dislocations than in glacial ice. © 1997 Optical Society of America

1. Introduction

AMANDA (Antarctic Muon and Neutrino Detector Array) is a U.S.–Germany–Sweden collaboration that is constructing an expandable facility deep in the South Pole ice cap to detect high-energy neutrinos from astrophysical sources.¹ A small fraction of muon-type neutrinos passing through the Earth will interact, converting into charged muons somewhere in the ice or in the bedrock below the ice. The muons typically have a range of a kilometer or more. Photomultiplier tubes (PMT's) embedded in the ice can detect the faint Cherenkov light emitted by muons passing through or near the AMANDA. If the arrival times and amplitudes of Cherenkov photons are recorded at many places in the ice volume, the direction of a muon track can be reconstructed. Electron-type neutrinos will typically convert into electrons that cause electromagnetic cascades whose light

emission pattern can be distinguished from that due to muons.

The ultimate performance of the AMANDA depends crucially on the optical properties of the ice. With a pulsed laser technique, the AMANDA collaboration has succeeded in making *in situ* measurements of the wavelength-dependent absorption and scattering coefficients at depths 800–1000 m,^{2,3} where the first stage of the array was deployed during the austral 1993–1994 summer. This stage consists of four vertical strings each with 20 PMT's spaced 10 m apart vertically, the strings forming an 80° sector of a circle of 30.4-m radius, with one string at the center and three strings on the circumference.

The method for separately extracting values of scattering and absorption lengths λ_s and λ_a as a function of wavelength with the pulsed laser method, together with results on both scattering and absorption, were reported in Refs. 2 and 3 and discussed in more detail in the accompanying paper.⁴ The reader is referred to Fig. 1 of Ref. 4 for a sketch showing the geometry for the pulsed laser method. In the present paper we frequently use the terms scattering coefficient or turbidity, $\tau \equiv 1/\lambda_s$, and absorption coefficient, $\alpha \equiv 1/\lambda_a$. Briefly, the method is as follows: Frozen into the deep ice is a three-dimensional array of light-collecting phototubes, near each of which is a diffusing ball attached to an optical

P. B. Price is with the Department of Physics, University of California at Berkeley, Berkeley, California 94720. L. Bergström is with the Department of Physics, University of Stockholm, Box 6730, S-11346 Stockholm, Sweden.

Received 8 July 1996; revised manuscript received 14 January 1997.

0003-6935/97/184181-14\$10.00/0

© 1997 Optical Society of America

fiber that runs to the surface. In a laboratory on the ice above the strings, one tunes a dye laser to any desired wavelength between approximately 410 and 610 nm, sends a pulse down one of the optical fibers that runs from the surface laboratory to a diffusing ball, and records the distribution of arrival times at any of the other PMT's. For each such run, a spherically symmetric pulse of monoenergetic photons emitted from a point source in the ice at time $t = 0$ and distance $d = 0$ undergoes a three-dimensional random walk with absorption, reaching a PMT at distance d with a time distribution that fits the following expression for photon density as a function of time:

$$u(d, t) = \frac{1}{(4\pi\kappa t)^{3/2}} \exp\left(-\frac{d^2}{4\kappa t}\right) \exp\left(-\frac{c_i t}{\lambda_a}\right). \quad (1)$$

The diffusion constant κ is equal to $c_i\lambda_e/3$, where $c_i = c/m$ = velocity of light in ice; m = the refractive index of ice; effective scattering length λ_e is related to λ_s as $\lambda_e = \lambda_s/(1 - \langle \cos \theta \rangle)$; and $\langle \cos \theta \rangle$, the mean value of the cosine of the scattering angle, takes into account the details of the angular distribution of scattered photons. For Rayleigh scattering, $\langle \cos \theta \rangle = 0$; for smooth, spherical bubbles, $\langle \cos \theta \rangle = 0.75$; for dust from aerosols, $\langle \cos \theta \rangle$ is typically in the range 0.8 to 0.9.

The results for scattering showed that ice at 800–1000-m depth is highly turbid, with effective scattering lengths λ_e that increase monotonically from approximately 40 cm at the shallowest depth to approximately 80 cm at the greatest depth.^{2,3} The magnitudes and depth dependence of λ_e were interpreted as due to residual air bubbles that slowly convert to almost invisible air-hydrate crystals at a rate that depends on depth, temperature, and time.⁵ With $\langle \cos \theta \rangle = 0.75$, the turbidity $\tau \equiv 1/\lambda_s$ decreases from 0.1 to 0.05 cm⁻¹ with depth, as shown in Fig. 1. In the present paper we discuss scattering that is due to bubbles and other mechanisms that are expected to become important at greater depths where bubbles are absent.

In Refs. 2 and 3 λ_a was measured at wavelengths 410–610 nm. The surprising result obtained was that, at the shortest wavelengths, λ_a is an order of magnitude greater than had been reported in measurements of ice grown in the laboratory.⁶ At the shortest wavelengths, λ_a was found to decrease with depth, a result that we attribute to absorption by dust, the concentration of which is predicted⁷ to increase with depth from ~900–1000 m and to reach a maximum at ~1050 m, corresponding to the time of the Last Glacial Maximum. These results are interpreted in detail in Ref. 4, which gives a fuller discussion of the process of photon diffusion with absorption.

2. Scattering by Air Bubbles

Figure 1 shows our recent measurements of turbidity $\tau = 1/\lambda_s$ at depths 820–980 m. If scattering by bubbles dominates, $\tau = n_{\text{bub}}\sigma_{\text{bub}}$, where n_{bub} = bubble

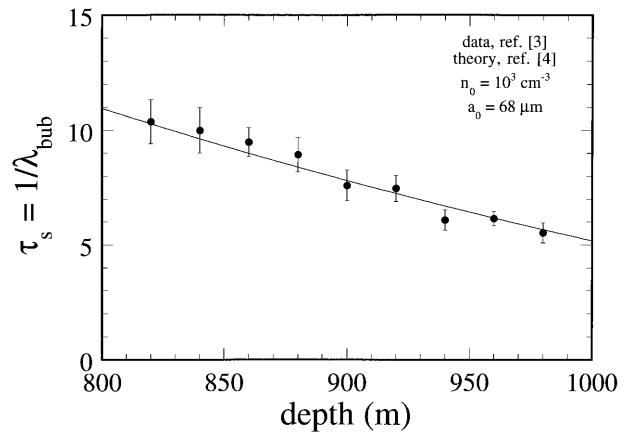


Fig. 1. Turbidity ($\tau = 1/\lambda_s$) as function of depth in South Pole ice for all wavelengths from 410–610 nm. Each point is a weighted mean of all measurements at that depth. The two parameters in the theory⁵ are n_0 , the initial number density of bubbles, and a_0 , the bubble radius at which conversion to the air-hydrate phase begins. Note that although the curve appears to be close to a straight line, it is concave and predicts a slower rate of disappearance of bubbles with depth than does a straight line extrapolation.

concentration and $\sigma_{\text{bub}} = \text{cross-sectional area } \pi r_{\text{bub}}^2$. A straight line fitted to the data would lead to the prediction that the contribution of bubbles to scattering would go to 0 at a depth of ~1150 m. There is, of course, no physical justification for the assumption that the product $n_{\text{bub}} r_{\text{bub}}^2$ goes linearly to 0 with depth. The rate of decrease of τ with depth is governed by the rate of conversion of bubbles into crystals of air hydrate,⁵ a solid phase with a refractive index almost identical to that of normal ice and thus almost invisible. The weak scattering by air-hydrate crystals is discussed in Section 4. The model for the conversion rate⁵ was able to fit data on air bubble sizes and concentrations in ice cores from both Byrd Station and Vostok, and the precise dependence of τ_{bub} on depth was predicted for South Pole ice with use of data in Ref. 2 for normalization. The curve in Fig. 1 was derived in Ref. 5. The model predicts that λ_s , due to bubbles, exceeds 10 m at a depth of 1400 m and exceeds 100 m at a depth of 1520 m. On this basis it was decided to deploy the next set of AMANDA PMT's at depths greater than 1500 m.

In the remainder of this paper we discuss all the other contributions to scattering, which at depths to 1000 m are swamped by the contribution of bubbles but which are expected to be significant at depths below ~1400 m, where $\lambda_{\text{bub}} > 10$ m. For each case we summarize the results in Table 1.

3. Thermal (Rayleigh + Brillouin) Scattering in Pure, Defect-Free Media

The Einstein–Cabannes expression for the turbidity that is due to thermal scattering in isotropic media includes both isobaric and adiabatic density fluctuations and takes into account the partial depolariza-

Table 1. Contributions to Turbidity of Ice at 436 nm and at depth ≥ 1500 m at the South Pole

Scattering Center	Modeled τ (cm^{-1})	Plausible Values of Parameters	Typical τ (cm^{-1})	Wavelength Dependence	Depth Dependence
Air bubbles	See Ref. 5	See Ref. 5	0.1 (800 m); 10^{-4} (1520 m)	None	Very strong ⁵
Intrinsic Rayleigh scattering	8×10^{-6}	pure H ₂ O	8×10^{-6}	λ^{-4}	None
Air-hydrate crystals	See Section 4	$\delta_{\text{rms}} = 1^\circ$	Very small	None	Constant at >1.4 km
Ice-ice boundaries	See Section 5	$\delta_{\text{rms}} = 0.12^\circ$	Very small	None	Slow increase
Vacancies + interstitials	$5 \times 10^{-27} n_{pt}$	$n_{pt} \leq 10^{16} \text{ cm}^{-3}$	$< 5 \times 10^{-11}$	λ^{-4}	None
Point impurities	$1 \times 10^{-27} n_{\text{imp}}$	$n_{\text{imp}} < 10^{15} \text{ cm}^{-3}$	$< 10^{-12}$	λ^{-4}	None
Impurity clusters	$< 10^{-27} n_{\text{imp}} v_{cl}$	$v_{cl} \approx 10^{4a}$	$< 10^{-8}$	λ^{-4}	None
Bare edge dislocations	$4 \times 10^{-13} n_{\text{disl}}$	$n_{\text{disl}} \approx 10^4 \text{ cm}^{-2}$	4×10^{-9}	λ^{-1}	None
Bare screw dislocations	$5 \times 10^{-15} n_{\text{disl}}$	$n_{\text{disl}} \approx 10^4 \text{ cm}^{-2}$	5×10^{-11}	λ^{-1}	None
Decorated dislocations	See Eq. (12)	10^7 atoms/bead; 10^4 beads/cm	3×10^{-5}	λ^{-4}	None
Acid in veins	See Eq. (17)	$a_v \approx 0.7 \mu\text{m}; f_a = 1$	1.4×10^{-3} (at all depths)	λ^{-1} to λ^{-2}	None
Undissolved salt	$3 \times 10^{-5} f_s c_{\text{salt}}$	$f_s = 1$	0.001 (< 0.9 km); 0.0033 (1.7 km)	λ^{-1} to λ^{-2}	Weak decrease with depth
Insoluble dust grains	$3 \times 10^{-5} c_{\text{dust}}$	15 ng/g (0.9 km); 280 ng/g (1.7 km)	0.0004 (< 0.9 km); 0.0084 (1.7 km)	λ^{-2}	Peaks at depths 1, 1.7, 2.4 km

^a v_{cl} = number of atoms per cluster.

tion of light scattered by nonspherical molecules:

$$\tau = \frac{8\pi^3}{3\lambda^4} \left(\rho \frac{\partial \epsilon}{\partial \rho} \right) T^2 \beta_T k T C_\tau, \quad (2)$$

where ϵ = dielectric constant, β_T = isothermal compressibility, ρ = density, and the Cabannes depolarization factor⁸ C_τ is $(6 + 3\Delta_u)/(6 - 7\Delta_u)$, with an optical anisotropy of scattering molecules given by

$$\Delta_u = \frac{\frac{(p_{11} - p_{12})^2}{c_{11} - c_{12}} + \frac{(p_{11} - p_{12})^2}{c_{11}}}{\frac{(p_{11} - p_{12})^2}{c_{11} - c_{12}} + 4 \frac{p_{12}^2}{c_{11}}}. \quad (3)$$

The p_{ij} and c_{ij} are photoelastic and elastic constants, respectively. (Δ_u can be determined experimentally by measuring the polarization of an initially unpolarized beam.) Entropy fluctuations give rise to the quasi-elastic Rayleigh central line, and pressure fluctuations give rise to acoustic waves and to the Brillouin satellite lines. The ratio $\tau_R/2\tau_B$ is equal to $(c_P/c_V - 1) = \beta_T/\beta_S - 1$ for isotropic, defect-free media. For gases, liquids, and amorphous solids, Eq. (2) can be approximated by

$$\tau_1 = \frac{32\pi^3}{3\lambda^4} \left(\frac{m}{\sigma} \frac{\partial m}{\partial T} \right) p^2 \beta_T k T C_\tau \approx \frac{8\pi^3}{3\lambda^4} (m^2 - 1)^2 \beta_T k T C_\tau, \quad (4)$$

where σ = volume expansion coefficient. Table 2 compares measured and calculated values of turbid-

Table 2. Thermal (Rayleigh + Brillouin) Scattering in Defect-Free Media at $\lambda = 436$ nm (units are 10^{-6} cm^{-1})

Type	Material	τ_{meas}	τ_1^a	τ_2^b	C_τ
Gases	Air	0.3	0.32	—	1.05
	CO ₂	0.79	0.78	—	1.13
Liquids and amorphous solids	Fresh water	40	34	—	1.34
	Seawater	52	45	—	1.34
	Silica fiber	40 ^c	4.4	—	1.26
	Benzene	600	330	—	2.37
Crystals	NaCl	2.3	7.5	7.5	1.03
	Quartz	2	6.3	11.6	1.26
	Ice	8 ^d	7.3	23	1.3
	Diamond	8	17	8.3	3.6

^a τ_1 calculated with Eq. (4).

^b τ_2 calculated with Eq. (5).

^c The anomalously high value is due to fluctuations frozen-in at glass transition temperature.

^d Measured at ~ 270 K; at 222 K at the South Pole, τ would be $\sim 6.6 \times 10^{-6} \text{ cm}^{-1}$.

ity due to thermal scattering for ice and a number of other media. Column 4 gives values of τ_1 calculated with Eq. (4). The only published measurement of Rayleigh scattering in ice is that of Raman.⁹ The other measurements are from Refs. 10 and 8. In all cases of interest to us, the intensity of Raman scattering is small (<20%) relative to Rayleigh + Brillouin scattering.

Scattering of light in crystals is not as straightforward as in amorphous media. In fact, the study of light scattering in crystals is a tool of solid-state physics that has occupied physicists for most of this century. The expressions for turbidity that is due to Rayleigh and Brillouin scattering depend on the polarization and directions of incidence and scattering of the light with respect to the crystal axes and are functions of p_{ij} and c_{ij} . Approximating a polycrystalline solid as an isotropic solid, one can combine the expressions for Rayleigh and Brillouin scattering of unpolarized light, replacing the elastic constants by isothermal and adiabatic compressibilities¹⁰:

$$\tau_2 = \frac{8\pi^3}{27\lambda^4} m^8 kT [\beta_T(p_{11} + 2p_{12})^2 + 9\beta_S p_{12}^2] C_T. \quad (5)$$

Column 5 of Table 2 gives values of τ_2 for crystalline solids. Because photoelastic constants have not been measured for ice, and because their values are correlated with the refractive index, we use values of the photoelastic constants for water,¹¹ which has nearly the same refractive index as ice. The wavelength dependence of the refractive index for ice,

$$m = 1.2956 \left(\frac{\lambda}{700 \text{ nm}} \right)^{-0.021735} \quad (6)$$

in the interval $200 \leq \lambda \leq 700 \text{ nm}$, changes the overall dependence of turbidity on wavelength for ice only from λ^{-4} to $\sim \lambda^{-4.17}$.

An intriguing and diagnostically useful aspect of light scattering is its sensitivity to the nature and concentration of defects in crystalline solids, a subject that we discuss in Section 6. Landsberg¹² showed that one could, to a large extent, distinguish defect scattering from intrinsic thermal scattering by exploiting the facts that the central Rayleigh-scattering line in a crystal containing defects is intensified (for most types of defects), whereas the Brillouin sidebands are not. After surveying a large number of samples of many crystal types, he found a few specimens of NaCl, diamond, and quartz with negligible defect scattering. His measurements of intensity for specific directions of incident and scattered light in those single-crystal specimens agreed with values calculated from theoretical expressions for the corresponding directions to within 3 to 30%. The reader is referred to Ref. 8 for a thorough discussion of those early Russian experiments and comparison of data with theory.

Comparison of columns 3, 4, and 5 in Table 2 indicates that the simple expression for τ_1 agrees quite well with measurements for gases, not quite as well

for liquids, and only within a factor of ~ 3 for crystalline solids. For the latter, the agreement is no better when the expression for τ_2 is used. For crystals, neither the measurements in column 3 nor the expressions for τ_1 and τ_2 include the subtleties and corrections taken into account by Landsberg.

Table 1 summarizes our estimates of the contributions at $\lambda = 436 \text{ nm}$ of various processes to scattering in bubble-free South Pole ice. These processes are discussed in detail in later sections. We chose 436 nm as the reference wavelength because, before the advent of lasers, most measurements were made with a low-pressure mercury lamp, for which the 435.8-nm line was chosen because of its narrowness.

We conclude this section by pointing out, in connection with the relative merits of fresh water, ocean water, and ice as media for imaging Cherenkov light from muons and electrons, that thermal scattering in ice at -50°C is approximately one sixth as great as in defect-free fresh water at 20°C and approximately one eighth as great as in seawater at 4°C . This stems from the fact that ice is crystalline whereas water is a liquid, as a consequence of which water exhibits greater density fluctuations than does ice. Thermal scattering in ice is reduced because the oxygen atoms occupy a lattice. Disorder in the positions of the hydrogen atoms around the oxygens leads to ice having greater thermal scattering than fully ordered crystals such as NaCl.

4. Scattering by Air Hydrates

At depths $z > 400 \text{ m}$ at South Pole temperature (-50°C at that depth), air bubbles in ice become unstable against transformation into a two-phase system consisting of isolated air-hydrate crystals with a cubic crystal structure immersed in a polycrystalline ice matrix with the hexagonal structure. At the wall of an air bubble, the air hydrate grows as a spherical shell that thickens as water molecules diffuse from the surrounding ice through the shell to react with air molecules. For a long time it was not understood why air bubbles and air-hydrate crystals coexisted in Antarctic ice over a depth interval of many hundreds of meters. It was shown recently that the rate of conversion from bubbles to air-hydrate crystals is limited not by the nucleation rate of the new phase but by the slow diffusion rate of water through solid air hydrate.⁵ In Ref. 5 the depth dependence of air bubble concentration and the depth dependence of λ_s were modeled with laboratory observations of the rate of diffusion-driven conversion of bubbles into the stable air-hydrate crystal phase. The dependence of age and temperature on depth in the ice was taken into account. The model fits the available data on bubbles in cores from Vostok and Byrd Station, explains why bubbles and air-hydrate crystals coexist in deep ice over a range of depths as great as $z = 0.8 \text{ km}$, and predicts that, at $z > 1.4 \text{ km}$ in South Pole ice, the contribution of bubbles to λ_s is negligible compared with other types of scattering.

Air-hydrate crystals are not completely invisible in

ice; their refractive index relative to hexagonal ice has been measured recently to be 1.0040 ± 0.00068 .¹³ Multiple small-angle scattering at boundaries between normal ice and air-hydrate crystals will degrade images of distant objects seen in deep ice and will limit the performance of AMANDA if the photomultipliers are placed too far apart. Here we briefly summarize the results of our work in collaboration with Price *et al.*,¹⁴ in which the trajectories of photons emitted at the Cherenkov angle along the trajectory of a muon were followed as they scattered at boundaries between normal ice and air-hydrate crystals.

From data of Uchida *et al.*,¹⁵ who studied air-hydrate crystals in the deep ice core from the Vostok station, we estimated the mean free path λ_s between air-hydrate crystals. Taking the mean volume concentration to be $V_{a-h} = 5 \times 10^{-4} \text{ cm}^3/\text{cm}^3$, independent of depth, and assuming spherical shapes and a rms radius of 50 μm , we infer a mean free path $\lambda_s = 13 \text{ cm}$ for air hydrates in South Pole ice. Integrating over impact parameters, we obtain a rms scattering angle $\delta_{\text{rms}} = 1^\circ$ for one encounter. This result is not sensitive to the shape of the clathrate. Although the distribution of single scatters is strongly non-Gaussian, after $\sim 10^2$ scatters the distribution is closely Gaussian, with the angular standard deviation

$$\sigma_\delta = \delta_{\text{rms}}(L_0/\lambda_s)^{1/2}, \quad (7)$$

where L_0 is the distance along the Cherenkov angle to the muon track. The distribution of transverse displacements is also nearly Gaussian, with the standard deviation in displacement

$$\sigma_d = \delta_{\text{rms}}(L_0/\lambda_s)^{3/2}\lambda_s/\sqrt{3}. \quad (8)$$

For $L_0 = 25 \text{ m}$ we estimate $\sigma_\delta \approx 13^\circ$ and $\sigma_d \approx 3.3 \text{ m}$.

We calculated the timing dispersion due to photons that are emitted from all points along a muon's trajectory and that scatter into a PMT. Absorption prevents the integral from diverging. The distribution of arrival times has a sharp peak that is due to photons emitted from the part of the muon track near the Cherenkov angle and a weak but broad component that is due to photons coming from the muon track far upstream.

For a muon passing close to one of the PMT's, one finds that the angular error is

$$\Delta\alpha \approx \frac{\tan \theta_C}{\tan^2 \theta_C + 1} \frac{c\Delta t}{mL_0}. \quad (9)$$

For $\lambda_a = 300 \text{ m}$, we find that even for a long distance such as $L_0 = 50 \text{ m}$, the fraction of photons scattered more than 1° is only around 6%, and the associated time delay is 8 ns, which is acceptably small.

The fraction of photons giving pointing errors larger than 1° is considerably less than would be expected from a Gaussian distribution of pointing errors with $\sigma_\alpha = 1^\circ$ per PMT (namely, 0.32). The conclusion is that the air-hydrate crystals by themselves do not cause severe problems for AMANDA.

As seen in Section 7, the effects of scattering by aerosols deposited into the ice pose a more serious problem.

5. Refraction (scattering) at Planar Interfaces between Two Ice Crystals

Ice has a hexagonal crystal structure and is birefringent. The ratio of refractive indices parallel to and perpendicular to the c axis is 1.0011 throughout the visible region.¹⁶ In the worst case of an isotropic distribution of c axes of ice crystals, the average ratio of refractive indices across an interface would be 1.0005. The number of scatters is L_0/D for a measurement distance L_0 and a mean crystal size D . For a depth of 1.5 km we assume $D = 0.4 \text{ cm}$, the same as measured in the Vostok ice core at the same depth.¹⁷ For an average ratio = 1.0005, the rms scattering angle per encounter $\delta_{\text{rms}} = 0.15$ degree. Fortunately, the c axes are not usually isotropically distributed. In response to stress, the c axes rotate as the ice deforms in response to gravity. Exploiting recent results of Alley *et al.*,¹⁸ who measured the distributions of angles between adjacent grains at various depths in the Byrd Station ice core, we assume a mean angle of 39° , from which we infer an average refractive index ratio ≈ 1.0004 . This leads to $\delta_{\text{rms}} = 0.12$ degree. For $L_0 = 25 \text{ m}$, there would be 6250 scatters, a net deflection of $\sim 10^\circ$ and a transverse displacement of $\sim 2.4 \text{ m}$. Thus the net small-angle scattering due to birefringence of ice is comparable to that due to air-hydrate crystals.

6. Scattering from Defects in Crystals

A. Isolated Point Defects (vacancies and impurity atoms)

Point defects increase the intensity of the Rayleigh line but do not affect the Brillouin sidebands.¹⁹ For individual point defects, scattering goes as λ^{-4} and depends on the change in electronic polarizability at a defect site, the elastic strain field around the defect that is due to size mismatch, the strain field that is due to the effective charge on the defect,²⁰ and the concentration of defects. Fredericks *et al.*,¹⁹ were the first to demonstrate the linear dependence of turbidity on concentration of point defects in a crystal. They grew KBr crystals doped with various concentrations of calcium and found that, in crystals quenched to avoid precipitation of Ca, the turbidity increased as $5.9 \times 10^{-7} \text{ cm}^{-1}$ per 10^{19} Ca^{2+} ions per cm^3 (at 488 nm).

The results of Fredericks *et al.* for quenched crystals are roughly consistent with the theory of Arora *et al.*,²⁰ who calculated values of turbidity due to vacancies, point impurities, and point impurity-vacancy complexes that depended on their polarizabilities and fell in the range

$$\tau_{pt} \approx (1 \text{ to } 60) \times 10^{-27} \text{ cm}^2 \times n_{pt}(\text{cm}^{-3})(436/\lambda)^4. \quad (10)$$

In ice at -10°C the densities of vacancies²¹ and self-interstitials²² are $\sim 10^{12} \text{ cm}^{-3}$ and $\sim 10^{16} \text{ cm}^{-3}$, respectively. Dissolved ions of acids and salts are present in South Pole ice at concentration $\sim 10^{14}$ to

10^{15} cm^{-3} .¹⁴ Their role is negligible unless they aggregate into clusters or veins, the consequences of which we discuss in Subsection 6.D. In laboratory ice^{6,23,24} the impurity concentration, though not measured, was probably higher by 1 or more orders of magnitude.

By far the dominant impurity in ice at the South Pole is $\sim 10^{19}$ molecules cm^{-3} of atmospheric gases. We have seen that at shallow depths these gases are concentrated in bubbles and at great depths they are enclathrated in air-hydrate crystals. At great depths the residual concentration of such gases as isolated molecular impurities in solution in the ice must be considerably less than 10^{19} cm^{-3} since the volume in air-hydrate crystals accounts roughly for all of the gas.¹⁵ Applying the theory of Arora *et al.*²⁰ to ice, we find that 10^{19} cm^{-3} of isolated gas molecules in the lattice increase scattering by less than 1%.

B. Precipitation of Point Defects into Clusters

In crystals the solubility of impurities is usually low at room temperature but increases rapidly with temperature. To take impurities into solution, one has to heat the crystal to dissolve them and then quench the crystal to a temperature low enough to immobilize them. During the 1950's a number of studies showed that the turbidity of ionic crystals was typically an order of magnitude greater than that due to thermal scattering in a perfect crystal. Theimer and Plint²⁵ showed that the concentration of individual point defects is generally far too low to account for the excess scattering. They pointed out that the turbidity would greatly increase if the distribution of defects were able to precipitate into clusters. Approximating clusters as spheres with radii a small enough for Rayleigh scattering to be valid ($q \equiv 2\pi a/\lambda \ll 1$), one can show that the turbidity increases as $V_{\text{cl}}^2 n_{\text{cl}}$, where V_{cl} = volume of cluster and n_{cl} = number density of clusters. This means that, for a fixed concentration of impurities, turbidity is proportional to the volume of a cluster or to the number of impurity atoms per cluster v_{cl} . This increase in turbidity was demonstrated beautifully by Fredericks *et al.*,¹⁹ who showed that if KBr crystals doped with 400 parts in 10^6 of Ca were slowly cooled so as to precipitate Ca clusters, the turbidity was approximately 1600 times greater than if they were quenched so as to maintain the Ca atoms in solution.

Arora *et al.*²⁶ used light scattering to study the formation of precipitates in NaCl doped with 400 parts in 10^6 of Pb^{2+} . They measured turbidities to $\sim 10^5$ times greater than in high-purity NaCl and presented evidence that precipitation of excess Pb could occur both homogeneously and along dislocations.

C. Bare Dislocation Lines

Sahoo *et al.*²⁷ derived expressions for the turbidity due to bare (undecorated) dislocation lines and showed that the main contribution is the elastic strain field, which leads to a value independent of temperature and inversely proportional to wave-

length. They estimated values of turbidity

$$\tau_{\text{disl}} \approx (4 \text{ to } 20) \times 10^{-13} \times n_{\text{disl}} (\text{cm}^{-2}) (436 \text{ nm}/\lambda) \quad (11)$$

for a variety of crystal types, where n_{disl} = number of dislocation lines cm^{-2} . Applying their expressions to ice, we estimate $\tau_{\text{disl}} \approx 4 \times 10^{-13} n_{\text{disl}}$ at $\lambda = 436 \text{ nm}$ for edge dislocations and $\sim 5 \times 10^{-15} n_{\text{disl}}$ for screw dislocations.

Measurements of n_{disl} for ice, using x-ray topography, gave values of $\sim 10^4$ lines cm^{-2} (Ref. 28) for single crystals from the Mendenhall Glacier, somewhat lower values for large zone-refined, nearly perfect single crystals,²⁹ and higher values 10^5 to 5×10^5 lines cm^{-2} for samples of polycrystalline ice grown under laboratory conditions.³⁰ We take as reasonable estimates that $n_{\text{disl}} \approx 10^4$ in both South Pole ice and Mendenhall Glacier ice and that the polycrystalline laboratory-grown ice on which previous absorption measurements were made^{6,24} has $n_{\text{disl}} \approx \text{few} \times 10^5$ lines cm^{-2} . (It is reasonable that the dislocation density should be low in well-annealed and aged crystals such as found in glacial ice and should be high in freshly grown polycrystalline ice.) We then estimate that $\tau_{\text{edge}} \approx 4 \times 10^{-9} (436/\lambda) \text{ cm}^{-1}$ for edge dislocations in South Pole ice and $\approx 10^{-7} (436/\lambda) \text{ cm}^{-1}$ for laboratory ice. The contribution to turbidity that is due to the elastic strain field around dislocations is thus negligible, even for laboratory ice. Moreover, it has the wrong wavelength dependence.

D. Precipitation of Impurities onto Dislocations: Beads on a String

Despite the fact that the intensity of light scattered by the strain fields of dislocations is very faint, dislocation lines in crystals (including ice³¹) with favorable values of the photoelastic constants have been imaged by means of either birefringence topography or light-scattering topography.³² Kataoka *et al.*³³ showed that the intensity of scattered light increases by a factor of more than 10^3 if the dislocations are decorated with precipitated impurity atoms. The strain field around an edge dislocation, being tensile along one side of the axis, is much more favorable for decoration than the torsional strain field around a screw dislocation. There is now a vast literature³⁴ on optical imaging of decorated dislocations in almost every type of transparent crystal as well as in semiconductors.

If the binding energy of solute atoms in the precipitate exceeds their binding energy in the dislocation core, decoration will take the form of beads on a string rather than of a uniform cylinder. In most crystals the decoration has been found by imaging techniques to be in discontinuous beads.³⁴ This leads to a λ^{-4} dependence of τ and a Rayleigh-type angular distribution ($1 + \cos^2 \theta$), whereas a dislocation with continuous decoration and length $\gg \lambda$ would scatter as $\sim \lambda^{-3}$ to $\sim \lambda^{-2}$, depending on the diameter of the decorated cylinder, and with a forward-peaked angular distribution (see Ref. 35 and Subsection 6.D). In calculating the turbidity τ_{decor} due to decorated dis-

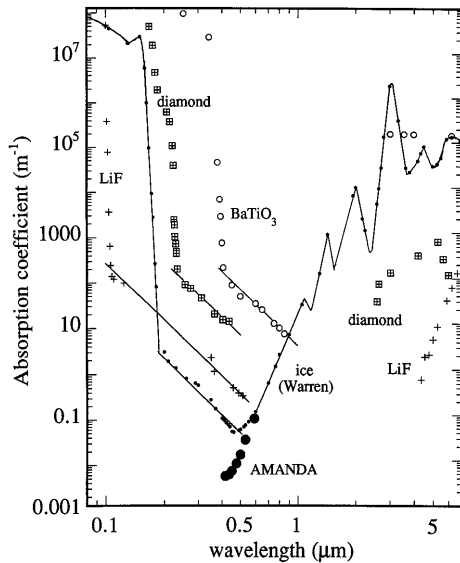


Fig. 2. Absorption spectra for ice and three other highly transparent solids. For the AMANDA data on South Pole ice the method was able to exclude the contribution of scattering to light attenuation. For the data on laboratory ice,^{6,23,24} LiF,³⁷ diamond,³⁸ and BaTiO₃,³⁹ the data are contaminated by scattering. This is evidenced by a truncation of the deep minimum by a line with a λ^{-4} dependence.

locations, we assume the number of atoms/bead = $\eta = 10^7$ and the number of beads/cm of dislocation = $\zeta = 10^4 \text{ cm}^{-1}$, based on direct transmission electron microscope observations of decorated dislocations in MgO.³⁶ The total length of dislocation lines per $\text{cm}^3 = L_{\text{disl}} \approx 3 n_{\text{disl}}$, assuming isotropic three-dimensional networks. Ignoring the contribution of dislocation strain fields and adding the contributions of individual beads, we obtain

$$\begin{aligned} \tau_{\text{decor}}(\text{cm}^{-1}) &= 1 \times 10^{-27} L_{\text{disl}} \eta^2 \zeta (436/\lambda)^4 \\ &= 3 \times 10^{-27} n_{\text{disl}} \eta^2 \zeta (436/\lambda)^4. \end{aligned} \quad (12)$$

E. Contamination of Some Absorption Spectra by Scattering from Defects

Figure 2 provides evidence that, near the minima in the absorption spectra of a number of transparent solids, the light is attenuated primarily by scattering from defects rather than by absorption. The absorption spectra of laboratory ice^{6,23,24} and of South Pole ice^{2,3} in and near the visible region are compared with spectra of LiF,³⁷ diamond,³⁸ and BaTiO₃.³⁹ To guide the eye, we have fitted λ^{-4} lines to the data at ~ 200 to 600 nm for these solids. We believe that the evidence for Rayleigh-type scattering in all but the South Pole ice is convincing.

In the case of LiF, a λ^{-4} line fits the data between 100 and 500 nm quite well over approximately 3 orders of magnitude of apparent absorption. A quantitative fit is achieved if the turbidity is a factor $\sim 10^3$ greater than due to thermal scattering. At a defect concentration of 30 parts in 10^6 , the average size of isolated clusters would have to be $\sim 4 \times 10^6$ atoms, which is

unreasonably high. However, using Eq. (12) with $L_{\text{disl}} = 5 \times 10^6 \text{ cm cm}^{-3}$, one can see that decorated dislocations account for the observed turbidity.

For both diamond and BaTiO₃ the abrupt change from a steeply falling Urbach tail to a λ^{-4} behavior, as shown by the lines through the data, is quite strong evidence for Rayleigh scattering from defects with dimensions much smaller than a wavelength. (For diamond, the defects turn out to be dislocation loops and nitrogen platelets; for BaTiO₃ they are nanoscale ferroelectric and ferroelastic domains.) A detailed discussion of scattering from specific nanoscale defects in transparent solids can be found in another paper.⁴⁰

With all these data in mind, it seems to us compelling that scattering from precipitated defects accounts for the λ^{-4} line through the data in Fig. 2 for laboratory ice at wavelengths between 200 and 500 nm . A factor $\sim 10^2$ increase above thermal scattering is needed. The strain fields of undecorated dislocations cannot account for the scattering because their contribution goes as λ^{-1} . Also, solid decorated cylinders do not give a good fit, because the dependence goes as $\sim \lambda^{-2}$. We therefore apply Eq. (12), which gives the turbidity that is due to dislocations decorated with discontinuous beads. Direct proof of the beads-on-string structure does not yet exist, because observations of dislocations in ice made with optical and x-ray topographic imaging do not have the resolution to detect a bead structure, and transmission electron microscopy has not been done on ice. However, we obtain a satisfactory fit to the data for laboratory ice^{6,24} if we use $L_{\text{disl}} = 4 \times 10^5 \text{ cm cm}^{-3}$, which is quite consistent with values observed in polycrystalline samples grown in the laboratory.³¹

Because of the ability of the pulsed laser technique to distinguish scattering from absorption, there would be no reason to encounter a segment showing a λ^{-4} dependence in future data for South Pole ice. However, if samples of it ever were to be studied with conventional laboratory techniques, a λ^{-4} line would probably show up. If so, we predict that such a line would appear at a level a factor 10 to 10^2 lower than for freshly grown ice because of its much lower dislocation density, as discussed in Subsection 6.C.

7. Scattering from Aerosol Particles Precipitated into South Pole Ice

A. Insoluble (Mineral) Dust Grains

An important contribution to scattering at depths $> 1450 \text{ m}$, where bubbles no longer contribute because they have completed the phase transition to air-hydrate crystals, is the presence of micrometer and submicrometer size grains deposited as aerosol nuclei. The concentrations of insoluble mineral grains, of salts of marine origin, and of acids (mainly sulfuric acid) have been studied as a function of depth in both a 2083-m Vostok core⁴⁰ and a 349-m South Pole core.⁴² Figure 3 gives histograms based on data in Table 2 of Ref. 41, showing the results in the three categories for the Vostok core, coarsely divided into average values

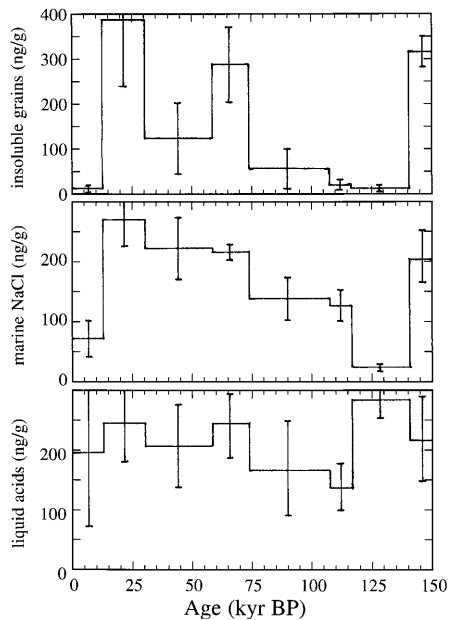


Fig. 3. Concentrations of insoluble mineral grains, marine salts, and liquid acids grouped in eight time epochs. Data are from the 2083-m deep Vostok core.⁴¹ The error bars are a measure of the variations within each of the eight segments of the core.

for eight time epochs. The concentrations in the shallow South Pole core are about half as great as in shallow parts of the Vostok core.⁴³ We use this factor 0.5 to scale data from Vostok to the South Pole.

Consider first the top histogram in Fig. 3, which shows large variations of the insoluble dust concentration with depth due to a correlation of the dust content of the atmosphere with global temperature. In addition to the coarse distribution in the upper histogram, we can also apply the higher-resolution stratigraphic data on dust obtained at Vostok⁴⁴ to the South Pole by employing a model of age versus depth developed in Ref. 7 for South Pole ice. This is illustrated in Fig. 4. The graph at the bottom of this figure shows for Vostok the concentration of insoluble dust as a function of age. The graph at the top gives the depth in South Pole ice inferred by use of the age versus depth model in Ref. 7 to convert the Vostok age scale at the bottom of the figure to depth. The three data points in the top graph show the values of absorption coefficient α measured with the pulsed laser method at a wavelength of 410 nm in three depth intervals.³ The increase in α with depth is attributed to an increase in dust concentration with depth. The good correlation of the depth dependence of α in the top graph (limited though the data may be) and the dust concentration in Vostok ice suggests that the age model for South Pole ice is satisfactory at least for the first 1000 m. Based on the Vostok data and our age model for South Pole ice, we expect additional broad peaks in the absorption due to dust to show up at depths of ~ 1700 and ~ 2430 m.

We now discuss ways to estimate τ_{dust} in South Pole ice. In Ref. 4 we developed a model with which to estimate τ_{dust} , and we briefly review it here. We

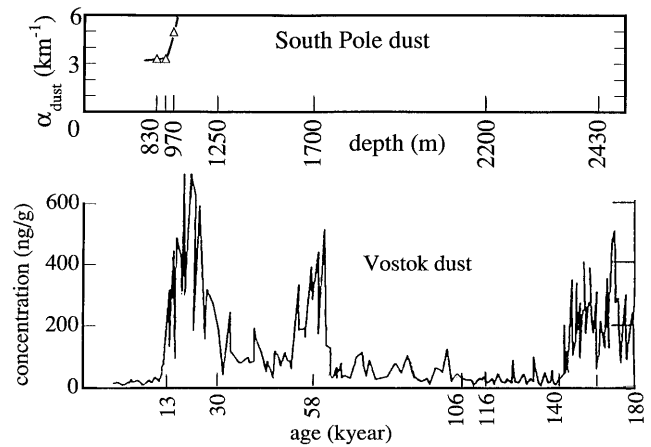


Fig. 4. Comparison of depth dependence of dust concentration measured in Vostok ice core samples with dust absorption coefficient α_{dust} inferred in South Pole ice from pulsed laser measurements. The bottom graph shows insoluble dust concentration in Vostok ice core samples as a function of age of the ice.⁴⁴ Using a model of age versus depth,⁷ the corresponding scale in terms of depth at the South Pole is shown in the top graph, together with values of α_{dust} measured at depths of 830, 900, and 970 m.³

used AMANDA measurements of absorption as a function of wavelength and depth to derive the contribution of dust to absorption at depths 800 to 1000 m. We represented the intrinsic absorption in dust-free ice in the red and near-IR by an exponential: $\alpha_{\text{int}}(\text{cm}^{-1}) = 1/\lambda_a = 81 \exp(\lambda_0/\lambda)$, with $\lambda_0 = 6.7 \mu\text{m}$, which gives an excellent fit to the data for laboratory ice at wavelengths ~ 600 to ~ 1200 nm. We assumed that the depth-dependent deviation from a pure exponential seen in the AMANDA data is due to an additive contribution of dust. Thus total absorption = intrinsic absorption + a depth-dependent contribution due to dust: $\alpha_{\text{tot}}(\lambda) = \alpha_{\text{int}}(\lambda) + \alpha_{\text{dust}}(z, \lambda)$, with $\alpha_{\text{dust}}(\lambda, z) = c_{\text{dust}}(z) \times \sigma_{\text{dust}}(\lambda)$, where c_{dust} = volume concentration of dust in ice. This implicitly assumes that the size distribution and nature of solid impurities are independent of depth and only the concentration changes. We concluded that α_{dust} decreases with wavelength and increases with depth in the interval $800 \leq z \leq 1000$ m, with typical values being $\sim (3.5 \text{ to } 5) \times 10^{-5} \text{ cm}^{-1}$, corresponding to $1/\tau_{\text{dust}} \approx 200$ to 300 m. We found the ratio of values of c_{dust} at 970 and 830 m to be ~ 1.4 , and the ratio of α_{dust} at the two depths also to be ~ 1.4 , independent of wavelength. The wavelength dependence of α_{dust} for the ice is not inconsistent with values obtained by Lindberg and Laude⁴⁵ for atmospheric dust at various locations. In the interval ~ 300 to ~ 700 nm, the Lindberg and Laude data fit quite well a dependence $\alpha_{\text{dust}} \propto \lambda^{-2}$. According to the Mie theory, the wavelength dependence weakens as the mean size of the dust distribution increases. For particles in the ocean, for example, the wavelength dependence is quite variable. In Table 1 we list for ice the dependence λ^{-2} as our best estimate.

To estimate τ_{dust} as a function of depth, we combine Mie-scattering theory with information about the size

distribution and mineral type of the dust, using the two approaches discussed below.

1. Analogy to Other Ice Cores

Royer *et al.*⁴⁶ have analyzed dust in ice cores from Dome C, using a scanning electron microscope to obtain number versus radius distribution, using a Coulter counter to obtain the volume distribution, and using laser nephelometry to obtain the angular distribution of light scattered from insoluble dust suspended in a melted ice sample. A disadvantage of all three methods is that melting the ice destroys information about scattering from salt and acids. Although all three methods have their weaknesses, Royer *et al.* were able to arrive at a consistent picture of the dust content as obeying a log normal distribution with a modal radius of 0.25 μm for the number-to-log radius size distribution. Using this size distribution and applying Mie theory, they fitted the angular distribution of scattered light reasonably well. A useful parameter characterizing the angular distribution is $\langle \cos \theta \rangle$, which they found to be ~ 0.9 . We independently calculated $\langle \cos \theta \rangle = 0.92$ for their angular distribution. They derived values of $\tau_{\text{dust}} = 3.5 \times 10^{-4} \text{ cm}^{-1}$ for samples from shallow depths (corresponding to the Holocene period), 10^{-3} cm^{-1} for samples at the Last Glacial Maximum, and $5 \times 10^{-4} \text{ cm}^{-1}$ for samples with an age of $3 \times 10^4 \text{ yr}$. Scaling from Dome C to the South Pole⁷ would reduce their values of τ_{dust} by a factor of ~ 2.5 , from which we obtain the estimate

$$\tau_{\text{dust}} = 1.4 \times 10^{-4} [c_{\text{dust}}(\rho_{\text{dust}}/\rho_{\text{ice}})/15 \text{ ng/g}], \quad (13)$$

where $\rho_{\text{dust}}/\rho_{\text{ice}}$ = the ratio of mass densities of an average mineral dust grain and of ice.

2. Evidence from South Pole Core and Aerosol Data

The second approach uses data shown in Fig. 5 on the size distribution of South Pole dust as input to our own Mie-scattering calculation. In Fig. 5, the data from Mosley-Thompson⁴⁷ and Gayley and Ram⁴⁸ were obtained by analyzing insoluble dust in ice cores taken at the South Pole at depths 100 to 349 m. The data from Parungo *et al.*⁴⁹ are one of a number of measurements she and other coworkers made of aerosol particles collected in the air above the South Pole.^{49,50} The particles she observed included marine salt grains and acid droplets, neither of which would have been detected by Gayley and Ram or Mosley-Thompson. In Fig. 5 we chose Parungo's distribution with the smallest modal radius, $\sim 0.04 \mu\text{m}$, and we multiplied the concentrations of the airborne aerosols in each radius interval by a constant factor 2000 to normalize them to the concentrations in ice. A consequence of this much smaller modal radius than the one reported for Dome C is that the angular distribution is more isotropic, with $\langle \cos \theta \rangle = 0.7$ for $\lambda = 500 \text{ nm}$ and ~ 0.74 for 350 nm, instead of the value 0.92 obtained for Dome C.

The result of our calculation for a log normal size

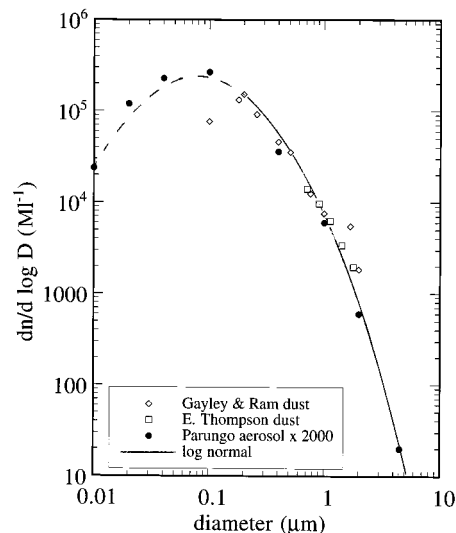


Fig. 5. Size distribution for dust at the South Pole. Mosley-Thompson⁴⁷ used filters of various sizes to obtain the size distribution of insoluble dust for diameters $> 0.7 \mu\text{m}$ in a core down to 349 m; Gayley and Ram⁴⁸ used scanning electron microscopy to measure diameters $\leq 2 \mu\text{m}$ of insoluble dust in the same core. Parungo *et al.*⁴⁹ collected aerosols in the air 20 m above the Clean Air Facility at the South Pole; their data include marine salt particles and acid droplets as well as insoluble grains. The log normal curve is dashed at values $< 2 \mu\text{m}$ to indicate uncertainty in the assumption that aerosols transfer into ice with efficiency independent of diameter.

distribution with modal radius = 0.04 μm is that the dependence of τ_{dust} on concentration of insoluble dust can be expressed as

$$\tau_{\text{dust}} = 4.5 \times 10^{-4} [c_{\text{dust}}(\rho_{\text{dust}}/\rho_{\text{ice}})/15 \text{ ng/g}]. \quad (14)$$

This is a more pessimistic estimate than the one based on the Dome C data [Eq. (13)]. Both τ_{dust} and $\langle \cos \theta \rangle$ are sensitive to the size distribution. The smaller the modal radius, the more closely the scattering approaches the Rayleigh regime, for which $\langle \cos \theta \rangle = 0$, and the more is the effective scattering per unit mass. The modal radius that fits the insoluble dust at Vostok is 0.3 μm .⁵¹ One can see from Fig. 5 that, if we were to ignore the aerosol data in fitting a log normal to the dust size measurements in Fig. 5, the modal radius would increase to $\sim 0.1 \mu\text{m}$, which is closer to the values 0.25 to 0.3 μm reported for Dome C and Vostok. There are three reasons for not weighting the South Pole aerosol data as strongly as the core data: The efficiency for precipitation of the aerosols to the surface may be a function of size; the marine salt grains and acid droplets that comprise a large fraction of the aerosols tend to have smaller sizes than the insoluble mineral grains; and the data of Parungo *et al.*⁵⁰ show that there is considerable seasonal variability in the modal radius of aerosol distributions, ranging from 0.04 to $\sim 0.2 \mu\text{m}$ in one year. The factor ~ 3 difference in values of τ_{dust} estimated in Eqs. (13) and (14) is a measure of the uncertainty in our knowledge of τ_{dust} .

B. Marine Salt Grains

We recently discussed the possibility that, in South Pole ice at a temperature as low as -50°C , the grains of various marine salts may remain solid indefinitely and scatter light.⁷ The solid-state physics is poorly understood, and experts are divided as to the extent to which salt grains survive as scattering centers over times $>10^4$ years. For simplicity we assume the same grain size distribution and refractive index for salt as for mineral grains and use f_s as a parameter representing the fraction of the salt that scatters, leading to the expression

$$\tau_{\text{salt}} = (0.3 \text{ to } 1.1) \times 10^{-3} \times f_s \times [c_{\text{salt}}(\rho_{\text{salt}}/\rho_{\text{ice}})/35 \text{ ng/g}]. \quad (15)$$

The factor 0.3×10^{-3} applies if one uses the approach in Subsection 7.A.1 and the factor 1.1×10^{-3} applies if one uses the approach in Subsection 7.A.2. The second histogram in Fig. 3 shows the depth dependence of the concentration of marine salt measured in the Vostok core.⁴¹ We assume a wavelength dependence similar to that of the insoluble mineral grains, $\sim\lambda^{-1}$ to λ^{-2} . The dependence on depth (and thus on epoch) is much weaker than is the case for the insoluble grains. Thus, when considered together, the salt + mineral grains show a weaker depth dependence than would the mineral grains alone.

C. Liquid Acid in Veins at Three-Crystal Boundaries

The bottom histogram in Fig. 3 shows the depth dependence of the concentration of mineral acids. The acid concentration is seen to be roughly independent of depth throughout the entire period from the present day back to 150,000 yr ago. This lack of dependence of concentration on depth can be used as a signature of scattering by acids in South Pole ice. These acids, which remain liquid at the lowest temperatures of South Pole ice, are precipitated into the ice mainly as hydrated submicrometer droplets. Sulfuric acid dominates. Using a scanning electron microscope equipped with a cryogenic stage and energy-dispersive x-ray analysis, Wolff *et al.*⁵² studied the distribution of sulfur and chlorine in an ice sample from the Antarctic Peninsula. They showed that between 40 and 100% (best estimate 90%) of the liquid sulfuric acid had collected in three-crystal boundaries called veins, whereas the chlorine showed no concentration in veins. Other research, using electrical conductivity as a diagnostic tool,⁵³ provides supporting evidence that acid-filled veins along three-crystal boundaries are a common feature of glacial ice. It is believed that, during compaction and crystal growth, instead of acid migrating through solid ice, two-crystal boundaries move, sweeping up ions such as SO_4^{2-} , which then migrate within the roughly planar boundaries until they reach veins.

To show that such veins are likely to contribute to light scattering in South Pole ice, we construct a quantitative model of the process. Let c_{acid} be the volume concentration of acid (primarily H_2SO_4) in the ice as a

result of precipitation; let m_{acid}/m be the ratio of refractive indices of acid and ice; let a_v be the radius of a vein; and let D be the average size of an ice crystal at the depth of interest. If the acid were distributed uniformly in two-crystal boundaries it would have a thickness of only ~ 0.1 nm and light would be unaffected by its presence. We thus let f_a be the fraction of acid that has collected into veins and will contribute to scattering. The problem is to calculate the cross section for scattering and the angular distribution of the light scattered by a network of veins.

The size of a vein is determined by thermodynamic considerations: The acid concentrates until it reaches the melting point at the local temperature of the ice.⁵³ For $T = -45^\circ\text{C}$, this corresponds to a density of 0.366 g/mL and a refractive index of $m_{\text{acid}} = 1.3725$. In Vostok the average acid concentration is ~ 220 ng/g, which leads to $c_{\text{acid}} = 110 \text{ ng/g} \times (0.915/0.366) = 2.75 \times 10^{-7} \text{ cm}^3/\text{cm}^3$ in South Pole ice. As a first estimate of mean crystal size in South Pole ice at a depth of 1500–2000 m, we take $D \approx 0.4$ cm, the same as in Section 5. By geometry and conservation of acid we obtain a vein radius

$$a_v(\mu\text{m}) = 0.68 f_a^{1/2} [D(\text{cm})/0.4] [c_{\text{acid}}(\text{cm}^3/\text{cm}^3)/2.75 \times 10^{-7}]^{1/2}. \quad (16)$$

Recall that f_a is the fraction of the acid that has concentrated in veins.

Wait⁵⁴ solved the problem of scattering of plane-polarized light by an infinite circular cylinder at oblique incidence. In view of the large uncertainties in f_a and D , we make two approximations that simplify the analysis: We let the crystals and vein structure be cubic in shape and let the light impinge on the ice along one of the vein directions. Thus light scatters from two thirds of the veins at normal incidence and not at all from the other one third. The total scattering coefficient τ_{vein} is then $n_1 \sigma_1$, where n_1 = the number density of crystals per unit length of veins $\approx 2/D^2$, and σ_1 = the cross section per unit length $= 2a_v Q$, where Q is a dimensionless effective cross section familiar in Mie theory. In terms of the Mie dimensionless size parameter, $\rho = 2q(m_{\text{acid}}/m - 1)$, where $q = 2\pi a_v/\lambda$, Q (cylinder) is plotted in Fig. 6, along with the calculated dependence of Q (sphere) on ρ . At small values of both q and ρ , Q for unpolarized light is given by

$$Q(\text{cyl}) = \pi^2 q^3 [(m_{\text{acid}}/m)^2 - 1]^2 / 16 + \pi^2 q^3 [(m_{\text{acid}}/m)^2 - 1]^2 / \{8[(m_{\text{acid}}/m)^2 + 1]\}^2. \quad (17)$$

Note that this is the analog of the q^4 dependence of Q for spheres in the Rayleigh regime. When the inequality $q \ll 1$ is not satisfied, Q for a cylinder can be expressed in terms of the Lommel–Weber function as $Q(\rho) = 2 + \pi \Omega_1(\rho)$. Q goes to 0 as ρ goes to 0 and goes to 2 at large ρ , after oscillating in much the same way as does Q for a spherical scatterer. Figure 6 shows the difference in wavelength dependence of the scattering for cylinders and spheres. For $m_{\text{acid}}/m = 1.04$, typical of acid in veins, Q begins to deviate from

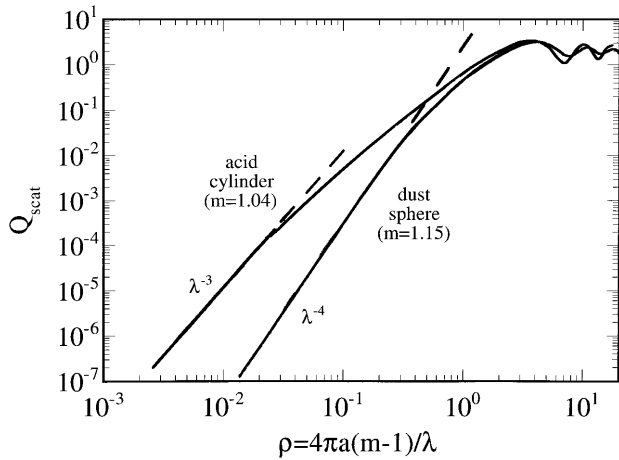


Fig. 6. Effective scattering factor Q for a sphere with $m = 1.15$ relative to ice and for a cylinder with $m = 1.04$. Here m refers to the ratio of refractive index of the scatterer relative to that of ice. At small values of ρ , Q goes as λ^{-4} for a sphere and as λ^{-3} for a cylinder.

the λ^{-3} line at values of ρ as small as $\sim 10^{-2}$, as can be seen in Fig. 6. For $m_{\text{dust}}/m = 1.15$, typical of a mineral in ice, Q begins to deviate from the λ^{-4} line at values of ρ above ~ 0.1 .

To find the turbidity that is due to acid in veins, we use

$$\tau_{\text{vein}}(\text{cm}^{-1}) = n_1 \sigma_1 = 4a_v Q/D^2. \quad (18)$$

For $D = 0.4$ cm and $f_a = 1$, we obtain $a_v = 0.68 \times 10^{-4}$ cm, and for $\lambda = 436$ nm, $Q = 0.4$ and $\tau_{\text{vein}} = 6.8 \times 10^{-4} \text{ cm}^{-1}$. For the above value of a_v , Q goes as $\sim \lambda^{-2}$. Note, however, that τ_{vein} and the wavelength dependence are rather sensitive to D . D might be a factor 2 or 3 larger than 0.4 cm, either because the rate of crystal coarsening depends on temperature, which is warmer at the South Pole than at Vostok, or because of the dependence of the rate on the concentration of soluble impurities such as Cl^- , which retard the motion of crystal boundaries. The concentration of Cl^- is roughly half as large at the South Pole as at Vostok and therefore contributes less to retardation. To take an example, for $D = 1$ cm, we would have $a_v = 1.7 \mu\text{m}$, $\rho = 1.95$, $Q = 2$, and $\tau_{\text{vein}} = 1.4 \times 10^{-3} \text{ cm}^{-1}$, with τ_{vein} going as $\sim \lambda^{-1}$.

For veins with $a_v \ll \lambda$, the angular distribution of scattered light would have forward-backward symmetry as in Rayleigh scattering, but for veins with $a_v \approx \lambda$ as in the present case, the distribution would be strongly forward peaked.⁵⁴

Acid-filled veins can make a sizable contribution to scattering in deep ice where bubbles are absent and the concentration of mineral dust is very small. Turbidity that is independent of depth and proportional to $\sim \lambda^{-1}$ to $\sim \lambda^{-2}$ would be attributable to scattering from veins.

8. Discussion

The contributions to scattering in South Pole ice are summarized in Table 1. One sees that at shallow depths bubbles completely dominate and that at $z >$

1500 m, acid would play an important role if $f_a \approx 1$, salt would play an important role if $f_s \approx 1$, and insoluble dust would play an important role if f_a and f_s were $\ll 1$. The relative roles of these major scattering centers can, in principle, be sorted out by careful measurements of the dependence of λ_s on wavelength and depth. For example, if future observations at depths ≥ 1500 m show a dependence on $\sim \lambda^{-1}$ to λ^{-2} and no depth dependence, one would conclude that acids play an important role, with $f_a \approx 1$; and if there are peaks in scattering at depths corresponding to global low temperatures (predicted at 1700 and 2300 m), one would know that insoluble dust plays a more important role.

If future measurements of scattering, at depths ≥ 1500 m, show neither a depth dependence nor a wavelength dependence, it will present an interesting challenge, as can be seen by examining the last two columns in Table 1. None of the types of scattering is large enough in magnitude and independent of wavelength and depth to dominate over the expected contributions of acid, salt, and mineral grains.

9. Conclusions

1. The pulsed laser method, applied by way of optical fiber to deep ice, provides a highly successful method of independently measuring absorption and scattering coefficients as a function of wavelength over the interval 410 to 610 nm. As a diagnostic tool of ice stratigraphy, it should be considered as a cost-effective method for remotely mapping bubble densities and, at depths where bubbles do not dominate, of dust concentrations in the Antarctic or Greenland ice pack. With a vertical spacing between phototubes of ~ 10 m it may be possible to resolve vertical structure in dust stratigraphy on a scale of a few tens of meters.

2. Most previous laboratory studies of absorption spectra in ice and other solids were vulnerable to scattering, which truncated the deep absorption minimum with a λ^{-4} contribution.

3. To further the understanding of the sources of scattering in deep Antarctic ice, we suggest two types of laboratory experiments: One should map defect structures such as dislocations and stacking faults in deep core samples with a cryogenic x-ray topographic method. One should also use laser nephelometry to study scattering in fresh core samples that show no evidence of secondary bubbles (i.e., those that are due to a phase transition of air hydrates back to bubbles). By comparing scattering in both solid and melted cores, one might be able to estimate the parameters f_s for salt grains and f_a for liquid acids.

4. Assuming that the age versus depth scale for South Pole ice is correct, the data in Fig. 4 suggest that the concentrations of mineral dust at depths 800 to 900 m are typical of the Holocene period and are as low as can be found at any depths. Only at depths ~ 2100 to ~ 2300 m do we expect to find such low dust concentrations.

5. The rise in α_{dust} in the interval 900–1000 m seems to correspond to the increase in dust concentration associated with the approach to the Last Glacial Maximum.

10. Glossary of Symbols Used

a	= radius of a precipitated cluster of point defects	α_{int}	= intrinsic absorption coefficient of ice
a_v	= radius of a cylindrical vein of acid	β_T, β_S	= isothermal compressibility, adiabatic compressibility
$c_i \equiv c/m$	= velocity of light in ice	δ_{rms}	= rms scattering angle of light from an air-hydrate crystal
c_{ij}	= elastic constants	Δ_u	= optical anisotropy of scattering molecules
$c_{dust}, c_{salt}, c_{acid}$	= volume concentration of dust grains, salt grains, and acid	ε	= dielectric constant
c_p, c_v	= specific heats at constant pressure and volume	ζ	= number of beads per unit length of decorated dislocation
C_τ	= Cabannes depolarization factor	η	= number of impurity atoms/bead on a decorated dislocation
d	= straight line distance from light source to receiver	κ	= diffusion coefficient
D	= mean diameter of ice crystal	λ	= wavelength
f_s, f_a	= fraction of salt not dissolved in ice, fraction of acid precipitated in veins	$\lambda_s, \lambda_a, \lambda_e$	= scattering length, absorption length, and effective scattering length
k	= Boltzmann constant	ν_{cl}	= mean number of atoms per cluster
L_{disl}	= total length of dislocation line per unit volume	ρ	= dimensionless size parameter in Mie theory
L_0	= distance along Cherenkov angle to the track of the light-generating muon	$\rho_{ice}, \rho_{dust}, \rho_{salt}$	= density of ice, dust, salt
m, m_{acid}, m_{dust}	= refractive index of ice, acid, and mineral dust	σ	= volume expansion coefficient
$n_{bub}, n_{pt}, n_{imp}, n_{cl}, n_1$	= number density of bubbles, vacancies/interstitials, impurities, clusters, ice crystals per unit length of veins	σ_{bub}, σ_1	= scattering cross section for a bubble, scattering cross section per unit length for an acid vein
n_{disl}	= number of dislocation lines threading a unit area	σ_{dust}	= absorption cross section for a dust grain
p_{ij}	= photoelastic constants	σ_δ, σ_d	= standard deviation of scattering angle, of lateral displacement
$q = 2\pi a/\lambda$	= dimensionless parameter in scattering theory	$\tau = 1/\lambda_s$	= turbidity
Q	= dimensionless effective cross section in Mie theory	τ_1	= turbidity due to thermal scattering in an amorphous medium
r_{bub}	= radius of a bubble	τ_2	= turbidity due to thermal scattering in a crystal
T	= temperature	$\tau_{bub}, \tau_{pt}, \tau_{disl}, \tau_{edge}, \tau_{decor}, \tau_{dust}, \tau_{salt}, \tau_{vein}$	= turbidity due to air bubbles, point defects, dislocations, edge dislocations, decorated dislocations, insoluble dust in ice, undissolved salt in ice, acid veins in ice
u	= photon density	τ_R, τ_B	= turbidity due to Rayleigh scattering, Brillouin scattering
V_{a-h}	= mean volume concentration of air-hydrate crystals in ice at high pressure	θ	= scattering angle
V_{cl}	= mean volume of a cluster of point defects	θ_C	= Cherenkov angle
z	= depth		
$\alpha = 1/\lambda_a$	= absorption coefficient		

L. Bergström acknowledges support from the Swedish Natural Science Research council and the Stockholm University–University of California, Berkeley exchange program. P. B. Price acknowledges support from National Science Foundation grant PHY-9307420 and from the Uppsala University–University of California Berkeley exchange program.

References

1. P. C. Mock, P. Askebjør, S. W. Barwick, L. Bergström, A. Bouchta, S. Carius, B. Erlandsson, A. Goobar, L. Gray, A. Hallgren, F. Halzen, H. Heukenkamp, P. O. Hulth, J. Jacobsen, S. Johansson, V. Kandhadai, A. Karle, I. Liubarsky, D. M. Lowder, T. C. Miller, R. Morse, R. Porrata, P. B. Price, A. Richards, H. Rubinstein, Ch. Spiering, Q. Sun, Th. Thon, S. Tilav, C. Walck, R. Wischniewski, and G. Yodh, "Status and capabilities of AMANDA-94," in *Proceedings of the 24th International Cosmic Ray Conference* (Istituto Nazionale di Fisica Nucleare, Rome, 1995), pp. 758–761; L. Gray, P. Askebjør, S. W. Barwick, L. Bergström, A. Bouchta, S. Carius, B. Erlandsson, A. Goobar, A. Hallgren, F. Halzen, H. Heukenkamp, P. O. Hulth, J. Jacobsen, S. Johansson, V. Kandhadai, A. Karle, I. Liubarsky, D. M. Lowder, T. C. Miller, P. C. Mock, R. Morse, R. Porrata, P. B. Price, A. Richards, H. Rubinstein, Ch. Spiering, Q. Sun, Th. Thon, S. Tilav, C. Walck, R. Wischniewski, and G. Yodh, "The design of a neutrino telescope using natural deep ice as a particle detector," in *Proceedings of the 24th International Cosmic Ray Conference* (Istituto Nazionale di Fisica Nucleare, Rome, 1995), pp. 816–819.
2. P. Askebjør, S. W. Barwick, L. Bergström, A. Bouchta, S. Carius, A. Coulthard, K. Engel, B. Erlandsson, A. Goobar, L. Gray, A. Hallgren, F. Halzen, P. O. Hulth, J. Jacobsen, S. Johansson, V. Kandhadai, I. Liubarsky, D. Lowder, T. Miller, P. C. Mock, R. Morse, R. Porrata, P. B. Price, A. Richards, H. Rubinstein, E. Schneider, Q. Sun, S. Tilav, Ch. Walck, and G. Yodh, "Optical properties of the South Pole ice at depths between 0.8 and 1 kilometer," *Science* **267**, 1147–1150 (1995).
3. P. Askebjør, S. W. Barwick, L. Bergström, A. Bouchta, S. Carius, E. Dalberg, B. Erlandsson, A. Goobar, L. Gray, A. Hallgren, F. Halzen, H. Heukenkamp, P. O. Hulth, S. Hundertmark, J. Jacobsen, V. Kandhadai, A. Karle, I. Liubarsky, D. Lowder, T. Miller, P. Mock, R. Morse, R. Porrata, P. B. Price, A. Richards, H. Rubinstein, E. Schneider, Ch. Spiering, O. Streicher, Q. Sun, Th. Thon, S. Tilav, C. Walck, R. Wischniewski, and G. Yodh, "UV and optical light transmission properties in deep ice at the South Pole," *Geophys. Res. Lett.* (1997).
4. AMANDA Collaboration, "Optical properties of deep ice at the South Pole: absorption," *Appl. Opt.* **36**, 4168–4180 (1997).
5. P. B. Price, "Kinetics of conversion of air bubbles to air hydrate crystals in Antarctic ice," *Science* **267**, 1802–1804 (1995).
6. T. C. Grenfell and D. K. Perovich, "Radiation absorption coefficients of polycrystalline ice from 400–1400 nm," *J. Geophys. Res.* **86**, 7447–7450 (1981).
7. AMANDA Collaboration, "On the age vs depth and optical clarity of deep ice at South Pole," *J. Glaciol.* **41**, 445–454 (1995).
8. I. L. Fabelinskii, *Molecular Scattering of Light* (Plenum, New York, 1968).
9. C. V. Raman, "Thermal opalescence in crystals and the colour of ice in glaciers," *Nature (London)* **111**, 13–15 (1923).
10. J. Tauc, "Highly transparent glasses," in *Optical Properties of Highly Transparent Solids*, S. S. Mitra and B. Bendow, eds. (Plenum, New York, 1975), pp. 245–260.
11. S. P. Clark, Jr., *Handbook of Physical Constants* (Geological Society of America, New York, 1966).
12. G. S. Landsberg, "Molekular lichtzerstreuung in festen Körpern. I. Lichtzerstreuung im kristallinen Quarz und ihre Temperaturabhängigkeit," *Z. Phys.* **43**, 773–778 (1927); "II. Abhängigkeit der Intensität des zerstreuten Lichtes von der Temperatur," **45**, 442–448 (1927).
13. T. Uchida, W. Shimada, T. Hondoh, S. Mae, and N. I. Barkov, "Refractive-index measurements of natural air-hydrate crystals in an Antarctic ice sheet," *Appl. Opt.* **34**, 5746–5749 (1995).
14. P. B. Price, P. Askebjør, S. W. Barwick, L. Bergström, A. Bouchta, S. Carius, B. Erlandsson, A. Goobar, L. Gray, A. Hallgren, F. Halzen, H. Heukenkamp, P. O. Hulth, J. Jacobsen, S. Johansson, V. Kandhadai, A. Karle, I. Liubarsky, D. M. Lowder, T. C. Miller, P. C. Mock, R. Morse, R. Porrata, A. Richards, H. Rubinstein, Ch. Spiering, Q. Sun, S. Tilav, C. Walck, A. J. Westphal, R. Wischniewski, and G. Yodh, "Optical properties of South Pole ice for neutrino astrophysics," in *Proceedings of the 24th International Cosmic Ray Conference* (Istituto Nazionale di Fisica Nucleare, Rome, 1995), pp. 777–780.
15. T. Uchida, T. Hondoh, S. Mae, V. Ya. Lipenkov, and P. Duval, "Air-hydrate crystals in deep ice-core samples from Vostok Station, Antarctica," *J. Glaciol.* **40**, 79–86 (1994).
16. H. Miller, "Physical properties of ice," in Vol. 1b of *Landolt-Börnstein Numerical Data and Functional Relationships in Science and Technology*, K.-H. Hellwege, ed. (Springer-Verlag, New York, 1982), pp. 494–507.
17. V. Ya. Lipenkov, N. I. Barkov, P. Duval, and P. Pimienta, "Crystalline texture of the 2083 m ice core at Vostok station, Antarctica," *J. Glaciol.* **35**, 392–398 (1989).
18. R. B. Alley, A. J. Gow, and D. A. Meese, "Mapping c-axis fabrics to study physical processes in ice," *J. Glaciol.* **41**, 197–203 (1995).
19. W. J. Fredericks, P. R. Collins, and D. F. Edwards, "Light-scattering cross sections of Ca^{2+} and the calcium-cation vacancy complex in KBr," *Phys. Rev. B* **35**, 2999–3002 (1987).
20. A. K. Arora, R. Kesavamoorthy, and D. Sahoo, "Light scattering by point defects and their complexes in ionic crystals," *J. Phys. C* **15**, 4591–4598 (1982).
21. N. H. Fletcher, *The Chemical Physics of Ice* (Cambridge U. Press, Cambridge, England, 1970).
22. A. Higashi, A. Fukuda, T. Hondoh, K. Goto, and S. Amakai, "Dynamical dislocation processes in ice crystal," in *Dislocations in Solids* (Yamada Science Foundation, Univ. of Tokyo Press, Tokyo, 1985), pp. 511–515.
23. S. G. Warren, "Optical constants of ice from the ultraviolet to the microwave," *Appl. Opt.* **23**, 1206–1225 (1984).
24. D. K. Perovich and J. W. Govoni, "Absorption coefficients of ice from 250 to 400 nm," *Geophys. Res. Lett.* **18**, 1233–1235 (1991).
25. O. Theimer and C. A. Plint, "Light scattering by nearly perfect crystals," *Ann. Phys.* **3**, 408–422 (1958).
26. A. K. Arora, R. Kesavamoorthy, A. K. Sood, G. Venkataraman, R. Krishnaswamy, and D. Sahoo, "Study of precipitation in NaCl:Pb^{2+} by light scattering and ultramicroscopy," *J. Phys. Chem. Solids* **45**, 69–77 (1984).
27. D. Sahoo, A. K. Arora, and R. Kesavamoorthy, "Elasto-optic contribution to light scattering from dislocations in insulating crystals," *J. Phys. C* **16**, 1687–1692 (1983).
28. A. Fukuda and A. Higashi, "X-ray diffraction topographic studies of dislocations in natural large ice single crystals," *Jpn. J. Appl. Phys.* **8**, 993–999 (1969).
29. S. J. Jones, "X-ray topographic evidence for prismatic dislocations in ice," *J. Appl. Phys.* **41**, 2738–2739 (1970).
30. S. J. Jones and N. K. Gilra, "X-ray topographical study of dislocations in pure and HF-doped ice," *Philos. Mag.* **27**, 457–472 (1973).

31. T. Gonda, H. Kakiuchi, and K. Moriya, "In situ observation of internal structure in growing ice crystals by laser scattering tomography," *J. Crys. Growth* **102**, 167–174 (1990).
32. N. Ming and C. Ge, "Direct observation of defects in transparent crystals by optical microscopy," *J. Crys. Growth* **99**, 1309–1314 (1990).
33. T. Kataoka, H. Ohji, K. Kishida, K. Azuma, and T. Yamada, "Direct observation of glide dislocations in a KCl crystal by the light scattering method," *Appl. Phys. Lett.* **56**, 1317–1319 (1990).
34. S. Amelinckx, *Solid State Physics*, supp. 6 (Academic, New York, 1964).
35. H. C. van de Hulst, *Light Scattering by Small Particles* (Wiley, New York, 1957), pp. 315–317.
36. G. D. Miles, "Observations of impurity precipitates in magnesium oxide single crystals by ultramicroscopy," *J. Appl. Phys.* **36**, 1471–1475 (1965).
37. T. Tomiki and T. Miyata, "Optical studies of alkali fluorides and alkaline earth fluorides in VUV region," *J. Phys. Soc. Jpn.* **27**, 658–678 (1969); E. D. Palik and W. R. Hunter, "Lithium fluoride," in *Handbook of Optical Constants of Solids*, E. D. Palik, ed. (Academic, New York, 1985), pp. 675–693.
38. D. F. Edwards and H. R. Philipp, "Cubic diamond," in *Handbook of Optical Constants of Solids*, E. D. Palik, ed. (Academic, New York, 1985), pp. 665–673.
39. C. Wong, Y. Y. Teng, J. Ashok, and P. L. H. Varaprasad, "Barium titanate (BaTiO_3)," in *Handbook of Optical Constants of Solids II*, E. D. Palik, ed. (Academic, New York, 1991), pp. 789–803.
40. P. B. Price and L. Bergström, "Enhanced Rayleigh scattering as a signature of nanoscale defects in highly transparent solids," *Philos. Mag. A* (1997).
41. M. R. Legrand, C. Lorius, N. I. Barkov, and V. N. Petrov, "Vostok (Antarctica) ice core: atmospheric chemistry changes over the last climatic cycle (160,000 years)," *Atmos. Environ.* **22**, 317–331 (1988).
42. S. Kirchner and R. J. Delmas, "A 1000 year glaciochemical study at the South Pole," *Ann. Glaciol.* **10**, 80–84 (1988).
43. M. Kumai, "Identification of nuclei and concentrations of chemical species in snow crystals sampled at the South Pole," *J. Atmos. Sci.* **33**, 833–841 (1976); R. Delmas, M. Briat, and M. Legrand, "Chemistry of South Polar snow," *J. Geophys. Res.* **87**, 4314–4318 (1982).
44. J.-R. Petit, L. Mounier, J. Jouzel, Ye. S. Korotkevich, V. I. Kotlyakov, and C. Lorius, "Palaeoclimatological and chronological implications of the Vostok core dust record," *Nature (London)* **343**, 56–58 (1989).
45. J. D. Lindberg and L. S. Laude, "Measurement of the absorption coefficient of atmospheric dust," *Appl. Opt.* **13**, 1923–1927 (1974); J. D. Lindberg, "Absorption-coefficient-determination method for particulate materials," *Appl. Opt.* **33**, 4314–4319 (1994).
46. A. Royer, M. De Angelis, and J. R. Petit, "A 30000 year record of physical and optical properties of microparticles from an east Antarctic ice core and implications for paleoclimate reconstruction models," *Climatic Change* **5**, 381–412 (1983).
47. E. Mosley-Thompson, Byrd Polar Research Center and Department of Geography, Ohio State University, Columbus, Ohio 43210 (personal communication, 1995).
48. R. I. Gayley and M. Ram, "Atmospheric dust in polar ice and the background aerosol," *J. Geophys. Res.* **90**, 12921–12925 (1985).
49. F. Parungo, E. Ackerman, W. Caldwell, and H. K. Weickmann, "Individual particle analysis of Antarctic aerosols," *Tellus* **31**, 521–529 (1979).
50. F. Parungo, B. Bodhaine, and J. Bortniak, "Seasonal variation in Antarctic aerosol," *J. Aerosol Sci.* **12**, 491–504 (1981).
51. M. De Angelis, M. Legrand, J. R. Petit, N. I. Barkov, Ye. S. Korotkevich, and V. M. Kotlyakov, "Soluble and insoluble impurities along the 950 m deep Vostok ice core (Antarctica)—climatic implications," *J. Atmos. Chem.* **1**, 215–239 (1984).
52. E. W. Wolff, R. Mulvaney, and K. Oates, "The location of impurities in Antarctic ice," *Ann. Glaciol.* **11**, 194–197 (1988).
53. E. W. Wolff and J. G. Paren, "A two-phase model of electrical conduction in polar ice sheets," *J. Geophys. Res.* **89**, 9433–9438 (1984).
54. J. R. Wait, "Scattering of a plane wave from a circular dielectric cylinder at oblique incidence," *Can. J. Phys.* **33**, 189–195 (1955).